JASA ARTICLE

Acoustophoresis in polymer-based microfluidic devices: Modeling and experimental validation[a)]

Fabian Lickert,[1,b)] Mathias Ohlin,[2,c)] Henrik Bruus,[1,d)] and Pelle Ohlsson[2,e)]

[1]*Department of Physics, Technical University of Denmark, DTU Physics Building 309, DK-2800 Kongens Lyngby, Denmark*
[2]*AcouSort AB, Medicon Village, S-223 81 Lund, Sweden*

ABSTRACT:

A finite-element model is presented for numerical simulation in three dimensions of acoustophoresis of suspended microparticles in a microchannel embedded in a polymer chip and driven by an attached piezoelectric transducer at MHz frequencies. In accordance with the recently introduced principle of whole-system ultrasound resonances, an optimal resonance mode is identified that is related to an acoustic resonance of the combined transducer-chip-channel system and not to the conventional pressure half-wave resonance of the microchannel. The acoustophoretic action in the microchannel is of comparable quality and strength to conventional silicon-glass or pure glass devices. The numerical predictions are validated by acoustic focusing experiments on 5-μm-diameter polystyrene particles suspended inside a microchannel, which was milled into a polymethylmethacrylate chip. The system was driven anti-symmetrically by a piezoelectric transducer, driven by a 30-V peak-to-peak alternating voltage in the range from 0.5 to 2.5 MHz, leading to acoustic energy densities of 13 J/m^3 and particle focusing times of 6.6 s. © *2021 Acoustical Society of America.*
https://doi.org/10.1121/10.0005113

I. INTRODUCTION

Polymer-based microfluidic chips offer a multitude of advantages compared to traditional glass-based devices. A big advantage of polymers is the ease of volume fabrication and the low cost per chip using well-established manufacturing processes such as micro-injection molding or hot embossing. Further processing, such as the creation of channel structures through micro-milling as well as polymer-polymer bonding, can be performed to complete the design. Those processes also bring great flexibility in terms of materials. Thermosoftening plastics such as polycarbonate (PC) or cyclic olefin copolymer (COC), as well as polymethylmethacrylate (PMMA) or polystyrene (PS), are widely seen in the context of microfluidics. The price per polymer chip falls more than an order of magnitude below the typical cost of glass-based devices. This offers a solution to establish acoustophoresis devices also outside academia for use in medical devices. In applications outside the research environment, the need for single use devices is rising. Applications such as blood-plasma separation in a point-of-care environment require clean and unused fluidic chips to avoid cross-contamination. Furthermore, lab-on-a-chip systems are becoming well-established solutions. For acoustophoresis to play a role in those systems, compatibility with existing polymer-based microfluidic platforms is a requirement.

While polymers are already broadly used in many areas of microfluidics,[1] there have been only a few research groups working with polymers in the field of acoustofluidics. Published work on polymer-based acoustofluidic devices, made of either PMMA or PS, includes separation of bacteria and blood cells,[2,3] platelet separation,[4] and purification of lymphocytes[5,6] as well as particle flow-through separation[7,8] and focusing.[9] A common problem of single channel devices, however, is the low throughput compared to similar glass or silicon devices. This may be caused by the fact that they typically are designed for an acoustic resonance between the channel walls as is the case for glass- or silicon-based devices. This assumption is not necessarily true for polymer-based devices where the difference in the acoustic impedance between the chip material and liquid, causing the acoustic reflection, may be much lower. An indication of this is the sometimes surprising optimal operation frequency.[10]

Moiseyenko and Bruus recently introduced the principle of whole-system ultrasound resonances (WSURs)[9] and contrasted it with the conventional use of bulk acoustic waves (BAWs) and surface acoustic waves (SAWs) in acoustophoresis devices. According to the WSUR principle, the optimal conditions for achieving acoustophoresis in polymer devices are obtained by considering the dimensions of the whole system and the corresponding whole-system resonances instead of attempting to base the acoustophoresis on local standing wave resonances excited locally inside the liquid of the microchannels. We base our analysis of acoustophoresis in polymer chips on the WSUR principle.

In this paper, we present a finite-element model for three-dimensional (3D) numerical simulations of polymer-based acoustofluidic devices and validate it experimentally. As a proof of concept, we model acoustophoresis of suspended microparticles in a specific microchannel embedded in a PMMA polymer chip and driven by an attached piezoelectric transducer at MHz frequencies. We validate the model experimentally and use it to explore some of the obstacles for efficient polymer-based acoustophoresis and to design an operational device. Our results show that the usual design rules of conventional glass-based devices do not apply for polymer-based chips. This especially holds true when comparing channel resonances in hard-walled glass devices with the WSUR modes found in polymer-based devices with acoustic impedances close to that of water.

In Sec. II, we introduce the geometry, the materials, and the design of the polymer-based acoustofluidic device. In Sec. III, we present the basic theory, including governing equations and boundary conditions, and its implementation in the numerical 3D finite-element model. We show the resulting fields of the chip at resonance in Sec. IV and define a metric for the efficiency of the acoustophoretic particle focusing as a function of frequency. The experimental setup and the fabricated polymer chip are described in Sec. V A, and in Sec. V B, we summarize our experimental findings on the focusing ability of the chip as a function of frequency. Finally, in Sec. VI, we conclude with a discussion of the presented results.

II. THE DEVICE

The design of our acoustofluidic device is following the design of typical glass-based BAW devices with a long straight channel used for acoustic particle separation.[11–13] As listed in Table I, the channel is rectangular with height $h_{ch} = 150\,\mu m$ and width $w_{ch} = 375\,\mu m$, which in a hard-wall channel would sustain a horizontal pressure half-wave at 2 MHz. In a polymer device governed by WSUR modes, a much different resonance frequency is found. The device consists of a polymer chip made from PMMA, containing a microfluidic channel. Actuation is performed using a piezoelectric lead-zirconate-titanate (PZT) transducer. The PZT transducer and the PMMA chip are coupled through a 20-μm-thin layer of glycerol [99% volume-per-volume (v/v) glycerol, 1% (v/v) water], a well-proven method that allows

TABLE I. The length (l), width (w), and height (h) of the chip (pmma), the channel (ch), the piezoelectric transducer (pzt), the groove (grv), and the glycerol coupling layer (glc).

Symbol	Value	Symbol	Value
l_{pmma}	50 mm	l_{ch}	40 mm
w_{pmma}	5 mm	w_{ch}	375 μm
h_{pmma}	1.18 mm	h_{ch}	150 μm
l_{pzt}	24 mm	w_{grv}	300 μm
w_{pzt}	8 mm	h_{grv}	65 μm
h_{pzt}	2 mm	h_{cpl}	20 μm

for long-time operation and access to simple exchange of chip and transducer.[14–16] Since the temperature of the device is kept constant in the experiments by using a Peltier-element feedback loop, we neglect thermal effects in the numerical modeling.

A sketch of the acoustofluidic device used in the modeling and experiments is shown in Fig. 1 and supplemented by Table I. For simplicity, the shown inlets and outlets were omitted in the modeling. To ensure an optimal anti-symmetric motion in the yz-plane, the top electrode of the transducer is split in two halves by cutting a small groove using a dicing saw along the x-direction and driven by respective alternating (AC) voltages with a 180° phase difference similar to the work reported in the literature.[9,17,18]

III. THEORY

A. Governing equations

In our simulations, we follow closely the theory presented by Skov et al.,[19] including the effective boundary layer theory by Bach and Bruus.[20] We consider a time-harmonic electric potential $\tilde{\varphi}(\mathbf{r}, t)$, which excites the piezoelectric transducer and induces a displacement field $\tilde{\mathbf{u}}(\mathbf{r}, t)$
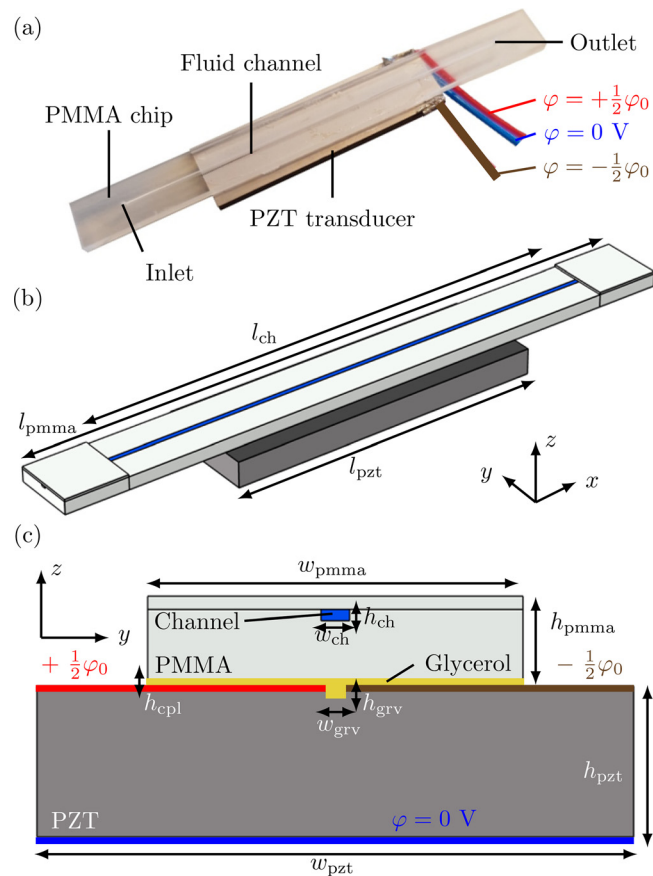

FIG. 1. (Color online) (a) A photograph of the acoustofluidic device, consisting of PMMA chip with a straight microfluidic channel, a piezoelectric transducer and a coupling layer made from glycerol. (b) Sketch of the 3D model, where the PMMA lid above the channel is removed to show the microchannel (blue) along the x axis. (c) Cross section of the 3D model in the vertical yz-plane. The coupling layer is visualized in yellow.

in the solids as well as an acoustic pressure $\tilde{p}_1(\boldsymbol{r}, t)$ in the fluid channel and in the coupling layer,

$$\tilde{\varphi}(\boldsymbol{r}, t) = \varphi(\boldsymbol{r}) \, e^{-i\omega t}, \tag{1a}$$

$$\tilde{\boldsymbol{u}}(\boldsymbol{r}, t) = \boldsymbol{u}(\boldsymbol{r}) \, e^{-i\omega t}, \tag{1b}$$

$$\tilde{p}_1(\boldsymbol{r}, t) = p_1(\boldsymbol{r}) \, e^{-i\omega t}, \tag{1c}$$

with the angular frequency $\omega = 2\pi f$. The time-harmonic phase factor $e^{-i\omega t}$ cancels out in the following linear governing equations. From first-order perturbation theory, it follows that the acoustic pressure $p_{1,\mathrm{fl}}$ in the fluid channel is governed by the Helmholtz equation with damping coefficient Γ_{fl},

$$\nabla^2 p_{1,\mathrm{fl}} = -\frac{\omega^2}{c_{\mathrm{fl}}^2}(1 + i\Gamma_{\mathrm{fl}}) \, p_{1,\mathrm{fl}},$$
$$\text{with } \Gamma_{\mathrm{fl}} = \left(\frac{4}{3}\eta_{\mathrm{fl}} + \eta_{\mathrm{fl}}^{\mathrm{b}}\right) \omega \kappa_{\mathrm{fl}}, \tag{2}$$

where c_{fl} is the speed of sound, ρ_{fl} is the density, $\kappa_{\mathrm{fl}} = (\rho_{\mathrm{fl}} c_{\mathrm{fl}}^2)^{-1}$ is the isentropic compressibility, and η_{fl} and $\eta_{\mathrm{fl}}^{\mathrm{b}}$ are the dynamic and bulk viscosity of the fluid, respectively. The acoustic velocity $\boldsymbol{v}_{1,\mathrm{fl}}$ of the fluid inside the channel can be expressed as a gradient of the pressure $p_{1,\mathrm{fl}}$ as

$$\boldsymbol{v}_{1,\mathrm{fl}} = -i \, \frac{1 - i\Gamma_{\mathrm{fl}}}{\omega \rho_{\mathrm{fl}}} \, \nabla p_{1,\mathrm{fl}}. \tag{3}$$

In the thin glycerol coupling layer, we cannot apply the effective boundary layer theory for the acoustic pressure $p_{1,\mathrm{cpl}}$ and velocity $\boldsymbol{v}_{1,\mathrm{cpl}}$.[20] So here, we implement the full set of governing equations,

$$\nabla \cdot \boldsymbol{v}_{1,\mathrm{cpl}} = i\omega\kappa_{\mathrm{cpl}} p_{1,\mathrm{cpl}}, \tag{4a}$$

$$\nabla \cdot \boldsymbol{\sigma}_{\mathrm{cpl}} = -i\omega\rho_{\mathrm{cpl}} \, \boldsymbol{v}_{1,\mathrm{cpl}}, \tag{4b}$$

$$\boldsymbol{\sigma}_{\mathrm{cpl}} = \eta_{\mathrm{cpl}} \left[\nabla \boldsymbol{v}_{1,\mathrm{cpl}} + (\nabla \boldsymbol{v}_{1,\mathrm{cpl}})^{\top} \right]$$
$$+ \left(\eta_{\mathrm{cpl}}^{\mathrm{b}} - \frac{2}{3}\eta_{\mathrm{cpl}} \right)(\nabla \cdot \boldsymbol{v}_{1,\mathrm{cpl}})\mathbf{I} - p_{1,\mathrm{cpl}}\mathbf{I}. \tag{4c}$$

Here, $\boldsymbol{\sigma}_{\mathrm{cpl}}$ is the viscous stress tensor, $\mathbf{I}$ is the identity tensor, $()^{\top}$ is the transpose, ρ_{cpl} is the density, κ_{cpl} is the isentropic compressibility, and η_{cpl} and $\eta_{\mathrm{cpl}}^{\mathrm{b}}$ are the dynamic and bulk viscosity of the coupling layer, respectively.

The equation of motion for the displacement field $\boldsymbol{u}$ of an elastic solid with density ρ_{sl} is Cauchy's equation

$$-\omega^2 \rho_{\mathrm{sl}} \, \boldsymbol{u} = \nabla \cdot \boldsymbol{\sigma}_{\mathrm{sl}}, \tag{5}$$

where $\boldsymbol{\sigma}_{\mathrm{sl}}$ is the stress tensor. The components σ_{ik} of the stress tensor are related by the stiffness tensor $\boldsymbol{C}$ to the strain tensor $\frac{1}{2}(\partial_i u_k + \partial_k u_i)$ and, for a linear isotropic elastic material, are written in the Voigt notation as

$$
\begin{pmatrix} \sigma_{xx} \\ \sigma_{yy} \\ \sigma_{zz} \\ \sigma_{yz} \\ \sigma_{xz} \\ \sigma_{xy} \end{pmatrix}
=
\left(\begin{array}{ccc|ccc}
C_{11} & C_{12} & C_{12} & 0 & 0 & 0 \\
C_{12} & C_{11} & C_{12} & 0 & 0 & 0 \\
C_{12} & C_{12} & C_{11} & 0 & 0 & 0 \\
\hline
0 & 0 & 0 & C_{44} & 0 & 0 \\
0 & 0 & 0 & 0 & C_{44} & 0 \\
0 & 0 & 0 & 0 & 0 & C_{44}
\end{array}\right)
\begin{pmatrix} \partial_x u_x \\ \partial_y u_y \\ \partial_z u_z \\ \partial_y u_z + \partial_z u_y \\ \partial_x u_z + \partial_z u_x \\ \partial_x u_y + \partial_y u_x \end{pmatrix}. \tag{6}
$$

Due to symmetry, the remaining three components of the stress are obtained by the relation $\sigma_{ik} = \sigma_{ki}$. The components $C_{ik} = C'_{ik} + iC''_{ik}$ of the stiffness tensor $\boldsymbol{C}$ are complex-valued to describe the weakly attenuated acoustics in the solid.

The electrical potential φ inside the PZT transducer is governed by Gauss's law for a linear, homogeneous dielectric with a zero density of free charges,

$$\nabla \cdot \boldsymbol{D} = \nabla \cdot (-\boldsymbol{\varepsilon} \cdot \nabla \varphi) = 0, \tag{7}$$

where $\boldsymbol{D}$ is the electric displacement field and $\boldsymbol{\varepsilon}$ the dielectric tensor. Furthermore, in PZT, the complete linear electromechanical coupling relating the stress and the electric displacement to the strain and the electric field is given by the Voigt notation as

$$
\begin{pmatrix} \sigma_{xx} \\ \sigma_{yy} \\ \sigma_{zz} \\ \sigma_{yz} \\ \sigma_{xz} \\ \sigma_{xy} \\ D_x \\ D_y \\ D_z \end{pmatrix}
=
\left(\begin{array}{ccc|ccc|ccc}
C_{11} & C_{12} & C_{13} & 0 & 0 & 0 & 0 & 0 & -e_{31} \\
C_{12} & C_{11} & C_{13} & 0 & 0 & 0 & 0 & 0 & -e_{31} \\
C_{13} & C_{13} & C_{33} & 0 & 0 & 0 & 0 & 0 & -e_{33} \\
\hline
0 & 0 & 0 & C_{44} & 0 & 0 & 0 & -e_{15} & 0 \\
0 & 0 & 0 & 0 & C_{44} & 0 & -e_{15} & 0 & 0 \\
0 & 0 & 0 & 0 & 0 & C_{66} & 0 & 0 & 0 \\
\hline
0 & 0 & 0 & 0 & e_{15} & 0 & \varepsilon_{11} & 0 & 0 \\
0 & 0 & 0 & e_{15} & 0 & 0 & 0 & \varepsilon_{11} & 0 \\
e_{31} & e_{31} & e_{33} & 0 & 0 & 0 & 0 & 0 & \varepsilon_{33}
\end{array}\right)
\begin{pmatrix} \partial_x u_x \\ \partial_y u_y \\ \partial_z u_z \\ \partial_y u_z + \partial_z u_y \\ \partial_x u_z + \partial_z u_x \\ \partial_x u_y + \partial_y u_x \\ -\partial_x \varphi \\ -\partial_y \varphi \\ -\partial_z \varphi \end{pmatrix}. \tag{8}
$$

J. Acoust. Soc. Am. **149** (6), June 2021

Lickert *et al.*   4283

As before, the remaining three components of the stress tensor are given by the symmetry relation $\sigma_{ik} = \sigma_{ki}$.

B. Boundary conditions between liquid, solid, and PZT

In the following, we state the boundary conditions of the fields on all boundaries and interfaces of the model. On the surfaces facing the surrounding air, we assume zero stress on the PMMA and the PZT as well as zero free surface charge density on the PZT. On the surfaces with electrodes, the PZT has a specified AC-voltage amplitude. On the internal surfaces between PMMA and PZT, the stress and displacement are continuous, and likewise on the fluid-solid interface, but here they are in the form of the effective boundary conditions derived by Bach and Bruus.[20] These effective boundary conditions include the viscous boundary layer analytically, and thus we avoid resolving these very shallow boundary layers numerically. The effective boundary conditions include the velocity $v_{sl} = -i\omega u$ of the solid (sl) and the complex-valued shear-wave number $k_s = (1+i)\delta_{fl}^{-1}$ of the fluid (fl), where $\delta_{fl} = \sqrt{2\eta_{fl}/(\rho_{fl}\omega)} \approx 0.5\,\mu m$ is the thickness of the boundary layer. In the coupling layer of height $h_{cpl} = 20\,\mu m$, the boundary layer thickness, $\delta_{cpl} = 12\,\mu m$, is nearly the same, so the effective boundary conditions do not apply. We therefore implement the full continuous conditions for stress and velocity at the interface of the solid (sl) and the coupling layer (cpl),

$$\text{PZT bottom}: \quad \varphi = 0, \tag{9a}$$

$$\text{PZT top}: \quad \varphi = \pm\frac{1}{2}\varphi_0, \tag{9b}$$

$$\text{PZT} - \text{air}: \quad \boldsymbol{D} \cdot \boldsymbol{n} = 0, \tag{9c}$$

$$\text{sl} - \text{air}: \quad \boldsymbol{\sigma}_{sl} \cdot \boldsymbol{n} = \boldsymbol{0}, \tag{9d}$$

$$\text{sl} - \text{fl}: \quad \boldsymbol{\sigma}_{sl} \cdot \boldsymbol{n} = -p_{1,fl}\boldsymbol{n} + ik_s\eta_{fl}(\boldsymbol{v}_{sl} - \boldsymbol{v}_{1,fl}), \tag{9e}$$

$$\text{fl} - \text{sl}: \quad \boldsymbol{v}_{1,fl} \cdot \boldsymbol{n} = \boldsymbol{v}_{sl} \cdot \boldsymbol{n} + \frac{i}{k_s}\boldsymbol{\nabla}_\parallel \cdot (\boldsymbol{v}_{sl} - \boldsymbol{v}_{1,fl})_\parallel, \tag{9f}$$

$$\text{cpl} - \text{sl}: \quad \boldsymbol{v}_{1,cpl} = \boldsymbol{v}_{sl} \tag{9g}$$

$$\text{sl} - \text{cpl}: \quad \boldsymbol{\sigma}_{sl} \cdot \boldsymbol{n} = \boldsymbol{\sigma}_{cpl} \cdot \boldsymbol{n}. \tag{9h}$$

We use the symmetry at the yz- and xz-planes to reduce the model to quarter size in the domain $x > 0$ and $y > 0$, allowing for finer meshing and/or faster computations. We apply symmetric boundary conditions at the yz-plane $x=0$ and anti-symmetry at the xz-plane $y=0$,

$$\text{Symmetry at } x = 0:$$
$$u_x = 0, \quad \sigma_{yx,sl} = \sigma_{zx,sl} = 0, \tag{10a}$$

$$v_{x,cpl} = 0, \quad \sigma_{yx,cpl} = \sigma_{zx,cpl} = 0, \tag{10b}$$

$$\partial_x p_{1,fl} = 0, \quad \partial_x \varphi = 0. \tag{10c}$$

$$\text{Anti-symmetry at } y = 0:$$
$$\sigma_{yy,sl} = 0, \quad u_x = u_z = 0, \tag{10d}$$

$$\sigma_{yy,cpl} = 0, \quad v_{x,cpl} = v_{z,cpl} = 0, \tag{10e}$$

$$p_{1,fl} = 0, \quad \varphi = 0. \tag{10f}$$

C. Acoustic energy density and radiation force

The space- and time-averaged acoustic energy density E_{ac}^{fl} in a fluid in a specified volume V_{fl} is given as the sum of the time-averaged kinetic and compressional energy,

$$E_{ac}^{fl} = \frac{1}{V_{fl}}\int_{V_{fl}}\left[\frac{1}{4}\rho_{fl}|\boldsymbol{v}_{1,fl}|^2 + \frac{1}{4}\kappa_{fl}|p_{1,fl}|^2\right]dV. \tag{11}$$

The acoustic radiation force $\boldsymbol{F}^{rad}$ acting on particles in the fluid is minus the gradient of the potential U^{rad}, specified for particles with radius a, density ρ_{ps}, and compressibility κ_{ps}, suspended in a fluid with density ρ_{fl} and compressibility κ_{fl},[21]

$$\boldsymbol{F}^{rad} = -\boldsymbol{\nabla}U^{rad}, \tag{12a}$$

$$U^{rad} = \pi a^3\left(\frac{1}{3}f_0\,\kappa_{fl}|p_{1,fl}|^2 - \frac{1}{2}f_1\,\rho_{fl}|\boldsymbol{v}_{1,fl}|^2\right), \tag{12b}$$

$$f_0 = 1 - \frac{\kappa_{ps}}{\kappa_{fl}}, \quad f_1 = \frac{2(\rho_{ps} - \rho_{fl})}{2\rho_{ps} + \rho_{fl}}, \tag{12c}$$

where f_0 and f_1 are the so-called acoustic monopole and dipole scattering coefficients, respectively.

D. Electrical impedance and admittance

The electrical impedance $Z = \varphi_0/I$ and admittance $Y = I/\varphi_0$ of the device are defined by the potential difference φ_0 between the two split top electrodes of the PZT [Eq. (9b)] and the electrical current I through one of these electrodes. Denoting the surface of the positive split electrode as $\partial\Omega_+$, we use the surface integral of the current density $\boldsymbol{J}$ to obtain $I = \int_{\partial\Omega_+}\boldsymbol{n}\cdot\boldsymbol{J}\,da = -i\omega\int_{\Omega_+}\boldsymbol{n}\cdot(\boldsymbol{D} + \epsilon_0\boldsymbol{\nabla}\varphi)\,da$,[22]

$$\begin{aligned}Y &= \frac{1}{Z} = \frac{I}{\varphi_0} = \frac{1}{\varphi_0}\int_{\partial\Omega_+}\boldsymbol{J}\cdot\boldsymbol{n}\,da \\ &= \frac{-i\omega}{\varphi_0}\int_{\partial\Omega_+}\big[e_{31}(\partial_x u_x + \partial_y u_y) + e_{33}\partial_z u_z \\ &\quad + (\varepsilon_0 - \varepsilon_{33})\partial_z\varphi\big]da.\end{aligned} \tag{13}$$

E. Material properties

The values of the material parameters are taken from the literature to match the validation experiments we have carried out. We study a suspension of 4.8-μm-diameter PS particles at a temperature of $T = 20\,°C$. To obtain neutral buoyancy, the liquid in the microchannel is chosen to be water mixed with a volume fraction of 16% iodixanol. The polymer is PMMA, the transducer is PZT, and the coupling

layer is glycerol. All parameter values used in the simulation are listed in Table II.

IV. RESULTS OF 3D SIMULATIONS

The simulations were implemented in the finite-element software COMSOL Multiphysics 5.5.[37] We closely follow the implementation of the numerical model given by Skov et al.,[19] where further details on the implementation are given. Using the symmetry conditions presented above, we solved a quarter of the actual 3D geometry and subsequently obtained the full solutions by mirroring the results along the xz- and yz-planes. The obtained fields are the potential φ in the PZT, the displacement $\boldsymbol{u}$ in all solid materials, and the acoustic pressure fields $p_{1,\mathrm{fl}}$ and $p_{1,\mathrm{cpl}}$ in the fluid and the coupling layer, respectively. In our time-harmonic simulations, we study the frequency range between 0.5 and 2.5 MHz, around the nominal 1-MHz resonance of the PZT transducer. The simulations were performed on the DTU high-performance cluster computer using shared-memory parallelism with a total of 16 cores and 160 gigabytes of random access memory. The meshing was done with a maximum element size of $h_{\mathrm{fl}}^{\max} = 70\,\mu\mathrm{m}$ in the fluid channel, $h_{\mathrm{pzt}}^{\max} = 280\,\mu\mathrm{m}$ in the PZT, and $h_{\mathrm{pmma}}^{\max} = 200\,\mu\mathrm{m}$ in the PMMA and vertically resolving the boundary layer in the coupling layer with five elements. The final mesh consists of about 100 000 mesh elements, corresponding to approximately 1.8×10^6 degrees of freedom. The computation time per frequency was about 20 min. We have performed a standard mesh-convergence study to ensure that our meshing is adequate.[19,38]

A. Electric admittance and acoustic energy density

The response of a piezoelectric transducer is usually studied by measuring the electrical impedance Z and finding its characteristic resonance and anti-resonance frequencies. The latter correspond to minima in the electrical impedance spectrum or maxima in the admittance spectrum $Y = 1/Z$ and are associated with maxima in the displacement of the transducer.[39] The simulated electrical admittance spectrum is shown in Fig. 2(a). The simulations show a maximum of the admittance at a frequency $f_{\mathrm{pzt}} = 1.13$ MHz, close to the 1-MHz resonance frequency specified by the manufacturer of the PZT transducer. This fair agreement is obtained despite our use of a split top electrode driven with an anti-symmetric voltage actuation, in contrast to the usual symmetrically driven full-top electrode mode.
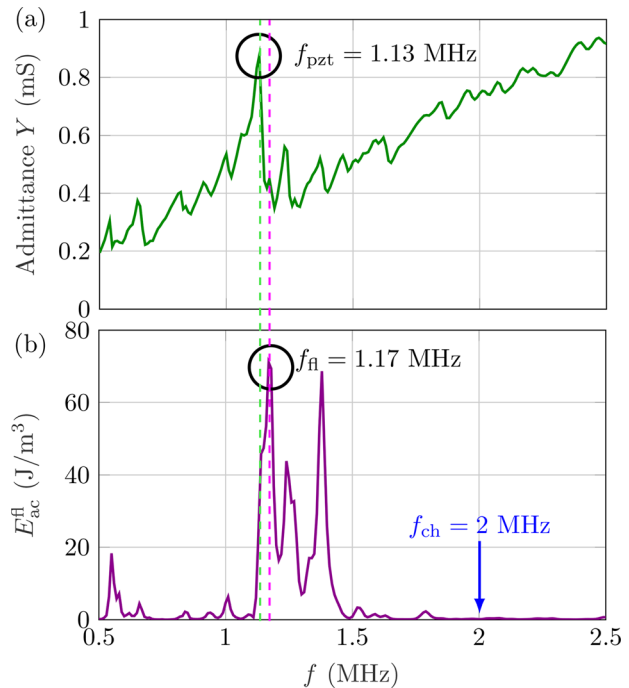
TABLE II. List of parameters at 20 °C used in the numerical simulation. Channel fluid [84% (v/v) water, 16% (v/v) iodixanol], 4.8-μm-diameter PS particles, glycerol solution [99% (v/v) glycerol, 1% (v/v) water], PMMA, and PZT. For PMMA $C_{12} = C_{11} - 2C_{44}$. For PZT $C_{12} = C_{11} - 2C_{66}$. ε_0 is the vacuum permittivity.

Parameter	Symbol	Value	Unit
Water-iodixanol mixture (Refs. 23 and 24)			
Mass density	ρ_{fl}	1050	kg m^{-3}
Speed of sound	c_{fl}	1482.3	m s^{-1}
Compressibility	κ_{fl}	433.4	TPa^{-1}
Dynamic viscosity	η_{fl}	1.474	mPa s
Bulk viscosity	$\eta_{\mathrm{fl}}^{\mathrm{b}}$	1.966	mPa s
PS (Ref. 25)			
Mass density	ρ_{ps}	1050	kg m^{-3}
Compressibility	κ_{ps}	238	TPa^{-1}
Monopole coefficient	f_0	0.479	—
Dipole coefficient	f_1	0	—
Glycerol (Refs. 26–28)			
Mass density	ρ_{cpl}	1260.4	kg m^{-3}
Speed of sound	c_{cpl}	1922.8	m s^{-1}
Compressibility	κ_{cpl}	214.6	TPa^{-1}
Dynamic viscosity	η_{cpl}	1.137	Pa s
Bulk viscosity	$\eta_{\mathrm{cpl}}^{\mathrm{b}}$	0.790	Pa s
PMMA (Refs. 29–36)			
Mass density	ρ_{sl}	1186	kg m^{-3}
Elastic modulus	C_{11}	$8.934 - \mathrm{i}0.100$	GPa
Elastic modulus	C_{44}	$2.323 - \mathrm{i}0.029$	GPa
PZT (Refs. 17, 19, and 36)			
Mass density	ρ_{sl}	7700	kg m^{-3}
Elastic modulus	C_{11}	$168 - \mathrm{i}3.36$	GPa
Elastic modulus	C_{12}	$110 - \mathrm{i}2.20$	GPa
Elastic modulus	C_{13}	$99.9 - \mathrm{i}2.00$	GPa
Elastic modulus	C_{33}	$123 - \mathrm{i}2.46$	GPa
Elastic modulus	C_{44}	$30.1 - \mathrm{i}0.60$	GPa
Coupling constant	e_{15}	$9.86 - \mathrm{i}0.20$	C m^{-2}
Coupling constant	e_{31}	$-2.8 + \mathrm{i}0.06$	C m^{-2}
Coupling constant	e_{33}	$14.7 - \mathrm{i}0.29$	C m^{-2}
Electric permittivity	ε_{11}	$828\varepsilon_0\,(1 - \mathrm{i}0.02)$	—
Electric permittivity	ε_{33}	$700\varepsilon_0\,(1 - \mathrm{i}0.02)$	—

FIG. 2. (Color online) Simulation results in the frequency range 0.5–2.5 MHz. (a) The electrical admittance Y of the mounted PZT transducer with a maximum at $f_{\mathrm{pzt}} = 1.13$ MHz. (b) The acoustic energy density $E_{\mathrm{ac}}^{\mathrm{fl}}$ in the channel with a maximum $E_{\mathrm{ac}}^{\mathrm{fl}} = 71\,\mathrm{J\,m}^{-3}$ at $f_{\mathrm{fl}} = 1.17$ MHz, far below the hard-wall resonance $f_{\mathrm{ch}} = 2$ MHz (blue).

J. Acoust. Soc. Am. **149** (6), June 2021

Lickert *et al.*   4285

In Fig. 2(b) is shown the simulated acoustic energy density E_{ac}^{fl} of the part of the fluid channel that is located directly above the PZT transducer. We find the maximum value to be $E_{ac}^{fl} = 71\,J\,m^{-3}$ at $f_{fl} = 1.17\,MHz$, which is close to, but 0.04 MHz higher than, the resonance frequency f_{pzt} found in the admittance spectrum.

As mentioned in Sec. II, had the microchannel of width $w_{ch} = 375\,\mu m$ had hard walls, it would have sustained an acoustic half-wave resonance at $f_{ch} = 2\,MHz$. In contrast, the simulations with PMMA walls show a strong acoustic resonance at $f_{fl} = 1.17\,MHz$, much lower than f_{ch}, but near the resonance frequency $f_{pzt} = 1.13\,MHz$ of the PZT transducer. As the resonance f_{fl} matches neither f_{ch} nor f_{pzt}, it is clearly a whole-system resonance.[9] This conclusion is supported by a closer inspection of the simulated fields at f_{fl} shown in Fig. 3 and in the corresponding videos in the supplementary material.[40]

Analyzing the displacement field $\boldsymbol{u}$, we note that the strongest displacement amplitude is obtained in the part of the PMMA located above the PZT [see Fig. 3(d)]. In particular, the highest displacement is found in the region above the fluid channel, which we will refer to as the channel lid in the following. We further note that the acoustic pressure forms a perfect standing anti-symmetric wave (albeit not a half-wave) with a vertical pressure nodal plane along the channel center in the region above the transducer. The amplitude of the pressure in the center of the fluid channel amounts to $p_{1,fl} = 755\,kPa$. This pressure amplitude decreases along the x-direction, toward both ends of the polymer chip. Finally, we observe a horizontal pressure wave in the glycerol coupling layer with an amplitude of about $p_{1,cpl} = 491\,kPa$.

The cross section of the acoustofluidic device, shown in Figs. 3(c) and 3(d), reveals an anti-symmetric motion of the sidewalls in the horizontal y-direction. The channel lid is performing a standing half-wave-like motion, perfectly in phase with the oscillation of the standing pressure wave inside the channel. An analysis of varying geometries of the polymer chip dimensions gave rise to the hypothesis that it is the motion of the sidewalls that is driving the channel resonance. To obtain a strong resonance, it is furthermore important to match the sidewall motion with the motion of the channel lid. Simulations so far have shown ideal results for inward motion of the sidewall, coupled with outward motion of the channel lid in one side of the channel. The width w_{ch} of the fluid channel and the thickness of the lid appear to set the frequency of the anti-symmetric standing wave in the lid, and by matching this frequency with that of the anti-symmetric sidewall resonance, high acoustic pressure amplitudes and gradients are produced in the channel. This whole-system resonance is governed by the dimensions of the entire geometry of the chip and is difficult to predict analytically.

B. Acoustophoretic focusability

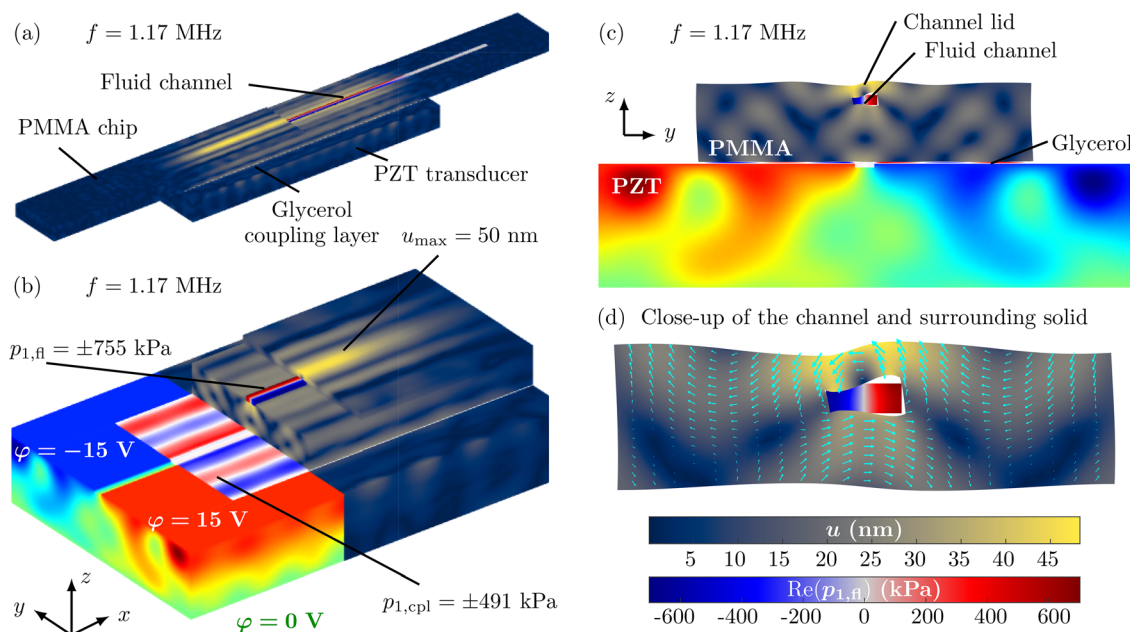To predict the acoustic focusing abilities of the device numerically, we compute the fraction of suspended particles

FIG. 3. (Color online) Numerical results of the 3D model, evaluated at a frequency of $f = f_{fl} = 1.17\,MHz$ and after mirroring the quarter-geometry results in the yz- and xz-symmetry planes back into the full geometry. (a) Color plot of the displacement magnitude u from 0 (dark blue) to 50 nm (yellow) and of the real part of the acoustic pressure p_1 in the fluid and in the coupling layer from minimum (blue) to maximum (red). (b) Cut-view of the simulated device showing color plots of the fields in the interior parts of the model, including the anti-symmetrically actuated electric potential φ in the PZT from $-15\,V$ (blue) to 15 V (red) and showing the different amplitudes of $p_{1,fl}$ and $p_{1,cpl}$. (c) Cross-section of the device in the yz-plane, which emphasizes the motion of the channel lid and the acoustic pressure inside the glycerol coupling layer. (d) Close-up view of the fluid channel and the adjacent lid. The displacement $\boldsymbol{u}$ (cyan vectors) has been scaled with a factor of 1000 to make the lid movement more visible. See the supplementary material for animations of the four views of the resonance mode (Ref. 40).

focused in the center region of the channel at different focusing times t as a function of frequency. We assume transverse acoustic focusing in the node of a half-wave pressure with the simulated amplitude, neglect acoustic streaming, and consider the case of a neutrally buoyant solution. In this case, the horizontal trajectory $y(y_0, t)$ of a particle at time t, starting at position y_0, is known analytically. Shifting the coordinate system so that the pressure node is at $y = \frac{1}{2} w_{ch}$ and the channel lies at $0 < y < w_{ch}$, we find that[41]

$$y(y_0, t) = \frac{w_{ch}}{\pi} \arctan\left[\tan\left(\pi \frac{y_0}{w_{ch}}\right) \exp\left(\frac{t}{t^*}\right)\right], \quad (14a)$$

$$t^* = \frac{3\eta_{fl} w_{ch}^2}{4\pi^2 \Phi a^2} \frac{1}{E_{ac}^{fl}}, \quad \text{with} \quad \Phi = \frac{1}{3} f_0 + \frac{1}{2} f_1, \quad (14b)$$

where Φ is the acoustic contrast factor and t^* is the characteristic focusing time. Using this expression, we then calculate the fraction of particles that are focused in a band of width w_{foc} around the nodal plane:

(1) Compute E_{ac}^{fl} from the numerical simulation and select the focusing band width w_{foc} and time t_{foc}.
(2) For a large number N of uniformly distributed initial positions y_0 for $0 < y_0 < \frac{1}{2} w_{ch}$, compute the final positions $y_{foc} = y(y_0, t_{foc})$ using Eq. (14).
(3) Count the number N_{foc} of particles inside the focusing band: $y_{foc} > \frac{1}{2}(w_{ch} - w_{foc})$.

The simulated focusability $\mathcal{F}_{sim}$ is then defined by

$$\mathcal{F}_{sim} = \frac{N_{foc}}{N}. \quad (15)$$

In our simulations, we chose $N = 10^5$ initial positions y_0 and a focusing bandwidth $w_{foc} = \frac{1}{10} w_{ch}$. We choose the focusing time to be the time it takes a given set flow rate Q_{flow} to sweep half the active volume $V_{fl} = l_{pzt} w_{ch} h_{ch}$ above the PZT transducer, $t_{foc} = \frac{1}{2}(V_{fl}/Q_{flow}) = l_{pzt} w_{ch} h_{ch}/2Q_{flow}$, which sets an upper limit to achieve good microparticle focusing in the center of the device for the given geometry. The resulting focusability $\mathcal{F}_{sim}$ is plotted versus frequency in Fig. 4(a) for the three flow rates $Q_{flow} = 10$, 50, and 100 μl/min, corresponding to the focusing times $t_{foc} = 4.0$, 0.8, and 0.4 s. The model predicts the best focusing of the device at the frequency $f_1 = 1.17$ MHz, identical to the frequency f_{fl} of Fig. 2(b) with the maximum acoustic energy density in the fluid channel. The acoustic pressure $p_{1,fl}$ and the acoustic radiation force $\boldsymbol{F}^{rad}$ at this frequency are shown in Fig. 4(b). Clearly, the simulated pressure is an antisymmetric standing pressure wave, for which the acoustic radiation force points toward the pressure node in the center of the channel, causing focusing in the center of the channel of suspended particles. Based on our simulations of the radiation force $\boldsymbol{F}^{rad} = (F_y^{rad}, F_z^{rad})$, we compute the figure of merit,[9] $R = \int_{V_{fl}} -\text{sign}(y) F_y^{rad} \, dV / \int_{V_{fl}} |F_z^{rad}| \, dV = 3.9$, which reveals that on average the horizontal focusing force F_y^{rad} is about 4 times larger than vertical force F_z^{rad} at the frequency
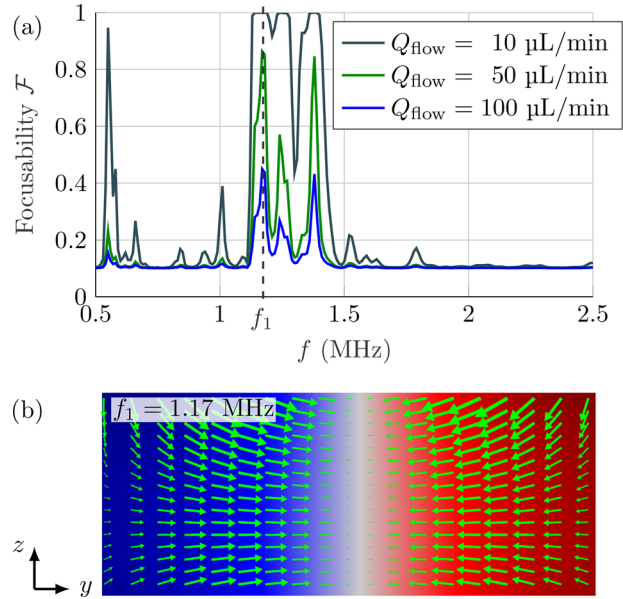

FIG. 4. (Color online) Simulation results. (a) Plot of the focusability $\mathcal{F}_{sim}$ versus frequency with a focusing bandwidth $w_{foc} = \frac{1}{10} w_{ch}$ and for the listed three flow rates Q_{flow}. (b) Color plot in the vertical channel cross section of the acoustic pressure $p_{1,fl}$ from -755 (blue) to $+755$ kPa (red) and the acoustic radiation force $\boldsymbol{F}^{rad}$ (green vectors) with a magnitude up to 5.5 pN for suspended 4.8-μm-diameter PS particles.

$f_1 = 1.17$ MHz, as can be seen qualitatively from the $\boldsymbol{F}^{rad}$ vectors (green) in Fig. 4(b). We therefore concentrate on the focusing in the y-direction toward the pressure node in this work.

V. EXPERIMENTAL SETUP AND RESULTS

A. Setup and procedure

The first step in the characterization of the acoustofluidic device was the measurement of the electrical admittance. The admittance spectrum $Y(f)$ between the two halves of the split top electrodes is measured using a Digilent (Pullman, WA) Analog Discovery 2 oscilloscope, applying the driving voltage to one of the top electrodes, grounding the other top electrode, and leaving the bottom electrode electrically floating. This is equivalent to adding a constant potential $+\frac{1}{2}\varphi_0$ to the simulated voltage configuration shown in Fig. 1(c). Observed differences between measured and simulated results for Y might be caused by a temperature sensor that is mounted on one side of the piezoelectric transducer but not included in the simulations. The piezoelectric transducer is coupled through a thin glycerol layer [99% (v/v) glycerol, 1% (v/v) water] to the microfluidic polymer chip. The thickness of this coupling layer was measured using a feeler gauge to be approximately 20 μm thick. For more information about the role of coupling layers, see Refs. 14–16 and 36.

In the following measurement, a frequency sweep at a fixed voltage amplitude of V = 15 V from 0.5 to 2.5 MHz was performed to analyze the experimental focusability of a neutrally buoyant suspension of 4.8-μm-diameter

J. Acoust. Soc. Am. **149** (6), June 2021

Lickert et al. 4287

fluorescent PS particles in a water-iodixanol mixture [84% (v/v) water, 16% (v/v) iodixanol]. The solution was pumped through the acoustofluidic device with a flow rate of 10 μl/min delivered by a syringe pump. Bright-field images were taken in steps of 5 kHz with a Hamamatsu (Hamamatsu City, Japan) Orca Flash 4.0 camera with 50 ms exposure time. At each frequency, the channel was flushed by briefly increasing the flow rate to 1800 μl/min for 0.1 s, followed by a waiting time of 45 s to stabilize the flow at a flow rate of 10 μl/min. Afterward, a series of ten images were taken with the piezoelectric transducer switched on and another ten images with the transducer switched off. The temperature during the experiment was kept constant at $T = 20\,°C$ using a Peltier element. From the obtained images, an average intensity profile $I_{exp}(y)$ across the channel was calculated at each frequency. The experimental focusability $\mathcal{F}_{exp}$ was then obtained from the integral of the intensity curve around the channel center divided by the integral across the entire channel, in analogy with $\mathcal{F}_{sim}$ in Eq. (15),

$$\mathcal{F}_{exp} = \frac{\int_{-1/2w_{foc}}^{1/2w_{foc}} I_{exp}(y)\,dy}{\int_{-1/2w_{ch}}^{1/2w_{ch}} I_{exp}(y)\,dy}. \qquad (16)$$

Here, we used $w_{foc} = \frac{1}{10} w_{ch}$ and thus determined the focusability into a band having the width of 10% of the channel width w_{ch}. In the experiments, we observed that at some frequencies there was a small offset from the channel center to the pressure node where the particles got focused. To facilitate the processing of the data in those cases where an intensity offset was observed, we integrated the intensity curve symmetrically around the point y_{max} of maximum intensity, thereby changing the limits of the integral in the numerator to $y_{max} \pm \frac{1}{2}w_{foc}$.

In the final experiment, we measured the acoustic energy density E_{ac}^{fl} using the same setup as described above: the neutrally buoyant solution, consisting of 84% (v/v) water, 16% (v/v) iodixanol, and fluorescent 4.8-μm-diameter PS beads is pumped through the microfluidic polymer chip at 10 μl/min. The same anti-symmetric actuation voltage with an amplitude of $\varphi_0 = \pm 15\,V$ was used, while the device temperature was kept constant at $T = 20\,°C$. However, unlike in the previous experiment, only selected frequencies, where some focusing had previously been observed, were studied in this experiment. A series of 600 images was recorded in time steps of $\Delta t = 20\,ms$, while the fluid flow was stopped. This was done to extract the acoustic energy density E_{ac}^{fl} around the main resonance frequency from the image series using the light-intensity method presented by Barnkob *et al.*[41]

B. Experimental results for the electrical admittance, particle focusability, and acoustic energy density

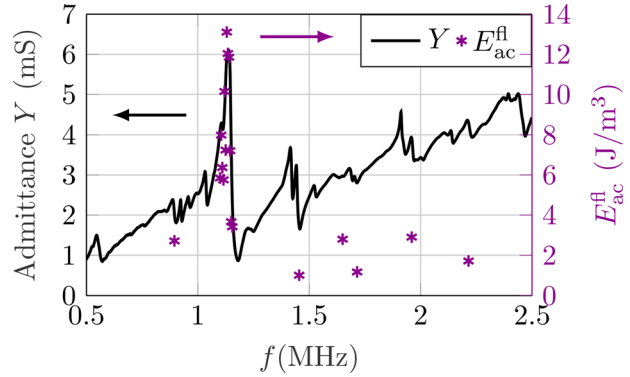We measured the electrical admittance Y as described in Sec. V A for a 1-MHz PZT transducer, after cutting a

FIG. 5. (Color online) The measured admittance spectrum Y (black) from 0.5 to 2.5 MHz using a floating bottom electrode and the corresponding acoustic energy density E_{ac}^{fl} (deep purple) obtained by the light-intensity method (Ref. 41) on a series of images recorded under stop-flow condition at selected frequencies showing good particle focusing. The resonance peak in the admittance is located at $f_Y = 1.14\,MHz$, closely coinciding with the frequency $f_{ac} = 1.13\,MHz$, where the energy density attains its maximum value $E_{ac}^{fl} = 13\,J\,m^{-3}$.

groove in the top electrode for anti-symmetric actuation. The admittance was measured while leaving the bottom electrode at a floating potential. The transducer was characterized while coupled to the microfluidic polymer chip. The measured electrical admittance Y and the corresponding acoustic energy density E_{ac}^{fl} measured at selected frequencies in the range from 0.5 to 2.5 MHz are shown in Fig. 5.

The admittance measurement exhibits a strong resonance peak at the frequency $f_Y = 1.14\,MHz$. Deviations from the nominal 1-MHz resonance are due to the groove cut into the transducer, the anti-symmetric actuation, and the load of the chip. Furthermore, we find that the maximum $E_{ac}^{fl} = 13\,J\,m^{-3}$ of the acoustic energy density is located close to this maximum of the measured admittance, in good agreement with what is reported in literature for typical glass-based devices.[39] This value of E_{ac}^{fl} corresponds to a focusing time of about $t_{foc} = 6.6\,s$ in the channel.

The results of the measurement of the particle focusability $\mathcal{F}_{exp}$ during continuous flow operation from 0.5 to 2.5 MHz are shown in Fig. 6(a). The frequency with the best focusing is $f_{foc} = 1.13\,MHz$, where about 60% of the particles are located within the center 10% of the channel width. Images of the particles inside the channel at this frequency are shown in Figs. 6(b) and 6(c) for the ultrasound switched off and on, respectively. See the supplementary material for a video showing particle focusing.[40]

C. Comparison with simulation results

The simulated values for the three key responses, the admittance Y, the focusability $\mathcal{F}$, and the acoustic energy density E_{ac}, agree fairly well with the experimental values. As shown in Fig. 7(a), the experimental and simulated admittance show the same behavior, and the frequencies of their respective maxima coincide within 0.9%, $f_Y^{exp} = 1.14\,MHz$ and $f_Y^{sim} = 1.13\,MHz$.

When comparing the measured maximum value $E_{ac}^{exp} = 13\,J\,m^{-3}$ of the acoustic energy density with the highest

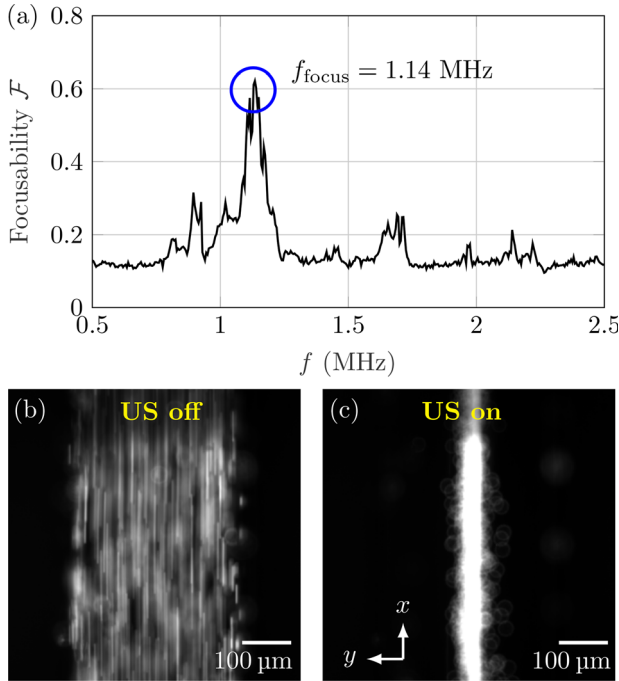4288   J. Acoust. Soc. Am. **149** (6), June 2021

Lickert *et al.*

FIG. 6. (Color online) (a) The experimental focusability $\mathcal{F}_{exp}$ versus frequency [see Eq. (16)], with a maximum 0.6 at $f_{foc} = 1.14\,\text{MHz}$. (b) Image of the particles in the channel with ultrasound (US) switched off. (c) Image of the particles in the channel with US switched on at the maximum $f_{foc} = 1.14\,\text{MHz}$. See the supplementary material for a video showing particle focusing (Ref. 40).
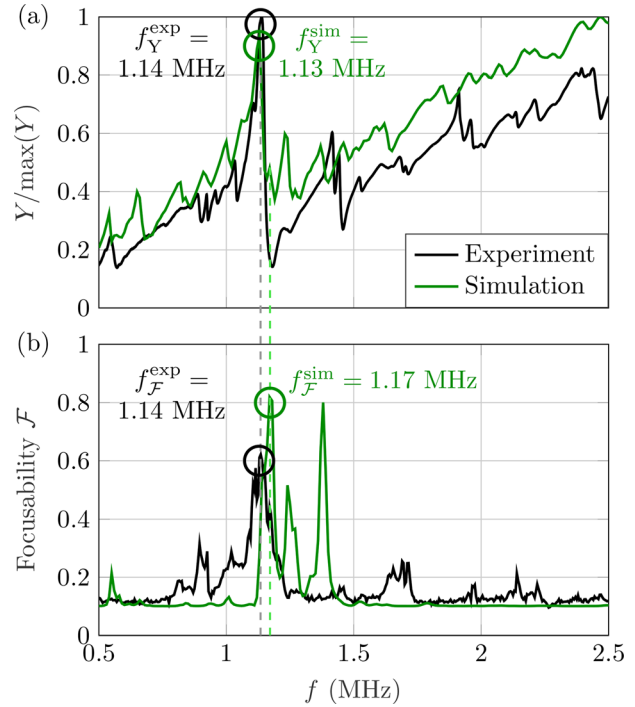

FIG. 7. (Color online) Top-view comparison between measured and simulated responses versus frequency from 0.5 to 2.5 MHz. (a) The measured (black) and simulated (green) electrical admittance Y showing closely coinciding main resonances at $f_Y^{exp} = 1.14\,\text{MHz}$ and $f_Y^{sim} = 1.13\,\text{MHz}$, respectively. (b) The experimental $\mathcal{F}_{exp}$ (black) and simulated $\mathcal{F}_{sim}$ (green) focusability, after calibrating the simulation to match the measured maximum of the acoustic energy density. Both focusabilities $\mathcal{F}$ show a maximum in the range from 0.6 to 0.8 and a small 2.6% deviation between the frequencies $f_{\mathcal{F}}^{exp} = 1.14\,\text{MHz}$ and $f_{\mathcal{F}}^{sim} = 1.17\,\text{MHz}$ of the respective maxima.

value $E_{ac}^{sim} = 71\,\text{J}\,\text{m}^{-3}$ computed in the simulation, we note that the simulation result is about 5.5 times higher than the experimental value. This difference most likely results from neglecting parts of the real system in our idealized simulation, such as the tubing, the mounting stage, and the inlet and the outlets, all which cause a reduction of the total energy of the real system. We furthermore observe another peak in the simulated acoustic energy density close to the frequency 1.4 MHz, which has not been observed experimentally. This likely stems from a small offset in the y-direction between the microfluidic channel and the piezoelectric transducer. This offset could not be implemented in the three-dimensional model, as it is breaking the symmetries utilized in the model. Simulations performed in two dimensions, however, have shown this peak to decrease drastically with small variations of the chip offset in y-direction, while the main peak at $f_{\mathcal{F}}^{sim} = 1.17\,\text{MHz}$ stays largely unaffected by this offset.

To compare the simulated and the experimental focusability, we use the standard procedure of calibrating the actuation voltage φ_0 in the simulation to ensure that $E_{ac}^{exp} = E_{ac}^{sim}$.[13] Using this calibrated actuation voltage, we recalculate the focusability with a flow rate $Q_{flow} = 10\,\mu\text{L/min}$ according to Eq. (15) and compare the resulting $\mathcal{F}_{sim}$ with $\mathcal{F}_{exp}$ plotted versus frequency in Fig. 7(b). We observe an upward frequency shift in the maximum of the simulated focusability curve, here by 2.6%. Both curves show a similar maximum focusability, namely $\mathcal{F}_{sim} = 0.82$ for the simulation and $\mathcal{F}_{exp} = 0.62$ in the experiment. These numbers

suggest good focusing of about 60%–80% of the particles. This value can be increased by lowering the flow rate or increasing the voltage amplitude on the transducer. We furthermore note that the highest measured focusability coincides with the global maximum in the measured admittance spectrum, as indicated by the gray-dashed line in Fig. 7. The simulated maximum in the focusability, however, relates to a small local maximum in the simulated admittance curve, approximately 40 kHz above the main admittance resonance $f_Y^{sim} = 1.13\,\text{MHz}$. This is indicated by the green-dashed line in Fig. 7. A maximum in the admittance spectrum typically relates to a maximum in the displacement of the piezoelectric transducer, which is driving the whole-system resonance. The small 2.6% deviation between the frequencies $f_{\mathcal{F}}^{exp}$ and $f_{\mathcal{F}}^{sim}$ of the focusability maximum likely stems from the idealized assumptions made for Eq. (14), such as using a perfect horizontal standing half-wave and neglecting the vertical component of the acoustic radiation force. Figure 4(b) and the figure of merit $R = 3.9$ computed in Sec. IV B show the limitations of this assumption.

VI. CONCLUDING DISCUSSION

We have presented a numerical model for 3D simulations of an acoustofluidic polymer device for particle

focusing, and we have validated it experimentally. Our 3D simulations predict good acoustic focusing at a frequency of $f_{\text{sim}} = 1.17\,\text{MHz}$, far below the half-wave resonance frequency $f_{\text{ch}} = 2\,\text{MHz}$ corresponding to a rigid hard-wall channel. Furthermore, we observe in our simulations that the resonance in the fluid channel is created through the motion of the sidewalls in phase with a standing wave motion of the channel lid. It is this whole-system resonance creating the standing pressure half-wave that in turn leads to good focusing at the specified frequency.

In Fig. 7(a), we find a good qualitative agreement between the simulated and measured electrical admittance spectrum of the device. Quantitatively, only a minor 0.9% shift in the two spectra was observed. More relevant for applications is the characterization of the ability of the polymer device to focus particles by acoustophoresis. To this end, we have introduced the focusability $\mathcal{F}$, which can be obtained both by simulation, $\mathcal{F}_{\text{sim}}$ in Eq. (15), and by experiments, $\mathcal{F}_{\text{exp}}$ in Eq. (16), thus enabling a good method to compare the two. The focusability $\mathcal{F}$ is the fraction of the incoming suspended particles, which are focused in the channel center for given focusing times or flow rates, enabling an estimate of the highest achievable flow rates to still maintain reasonable focusing at a selected frequency. Whereas in Fig. 7(b), we observe a small offset of 2.6% between the measured and simulated focusability, $\mathcal{F}_{\text{exp}}$ and $\mathcal{F}_{\text{sim}}$ exhibit the same focusing behavior and yield a similar maximum value of $\mathcal{F} = 0.6$–0.8, meaning that 60%–80% of the particles inside the channel are focused in the center 10% of the channel width.

By studying the electrical admittance, we find both in our simulation and in our experiment that the frequency of the admittance maximum closely coincides with the frequency of the focusability maximum. Both the resonance of the piezoelectric transducer and the whole-system resonance are governed by the dimensions of the transducer itself and the whole acoustofluidic device, respectively. Whereas the resonance frequency of the piezoelectric transducer is tunable through the height of the transducer, precisely predicting and manipulating the frequency of the WSUR is a more challenging task and requires numerical simulations. Matching this WSUR with the intrinsic resonance frequency of the transducer, however, would be ideal.

Another approach is to numerically find a design yielding a WSUR at the admittance resonance frequency of the selected piezoelectric transducer. The estimate that can be made based on numerical simulations, however, is only as good as the accuracy of the underlying material parameters. Whereas the mechanical and acoustic properties of glass and silicon are well studied and well reported in literature, it is a challenging task to obtain reliable material parameters for different polymer grades. This especially holds true for data on the transverse speed of sound and attenuation, which are required to compute the complex-valued stiffness coefficient C_{44}.

Further studies and measurements beyond the presented proof-of-concept example of the precise properties of the materials in use will increase the accuracy of our simulation model. Currently, we are working on characterizing various polymers for their applicability as base material in acousto-fluidic devices. To fully model the experimental device, fluid connectors and tubing, as well as the clamping of the device in the used measurement setup, need to be considered. With our simulation model, however, we obtained a reliable technique to make predictions on the applicability of polymer-based devices for particle focusing applications.

The existing model can be used for further optimizations of the design, to yield higher acoustic energy densities and therefore in turn enable flow rates higher than the reported $Q_{\text{flow}} = 10\,\mu\text{l/min}$. Scaling up the flow rate by 1 or 2 orders of magnitude seems possible and would make polymer-based acoustofluidic devices competitive with other particle focusing and separation solutions.

ACKNOWLEDGMENTS

[1]E. K. Sackmann, A. L. Fulton, and D. J. Beebe, "The present and future role of microfluidics in biomedical research," Nature 507(7491), 181–189 (2014).

[2]R. Silva, P. Dow, R. Dubay, C. Lissandrello, J. Holder, D. Densmore, and J. Fiering, "Rapid prototyping and parametric optimization of plastic acoustofluidic devices for blood-bacteria separation," Biomed. Microdev. 19(3), 70 (2017).

[3]P. Dow, K. Kotz, S. Gruszka, J. Holder, and J. Fiering, "Acoustic separation in plastic microfluidics for rapid detection of bacteria in blood using engineered bacteriophage," Lab Chip 18(6), 923–932 (2018).

[4]Y. Gu, C. Chen, Z. Wang, P.-H. Huang, H. Fu, L. Wang, M. Wu, Y. Chen, T. Gao, J. Gong, J. Kwun, G. M. Arepally, and T. J. Huang, "Plastic-based acoustofluidic devices for high-throughput, biocompatible platelet separation," Lab Chip 19, 394–402 (2019).

[5]C. Lissandrello, R. Dubay, K. T. Kotz, and J. Fiering, "Purification of lymphocytes by acoustic separation in plastic microchannels," SLAS Technol. 23(4), 352–363 (2018).

[6]R. Dubay, C. Lissandrello, P. Swierk, N. Moore, D. Doty, and J. Fiering, "Scalable high-throughput acoustophoresis in arrayed plastic microchannels," Biomicrofluidics 13(3), 034105 (2019).

[7]I. González, M. Tijero, A. Martin, V. Acosta, J. Berganzo, A. Castillejo, M. M. Bouali, and J. L. Soto, "Optimizing polymer lab-on-chip platforms for ultrasonic manipulation: Influence of the substrate," Micromachines 6(5), 574–591 (2015).

[8]C. Yang, Z. Li, P. Li, W. Shao, P. Bai, and, and Y. Cui, "Acoustic particle sorting by integrated micromachined ultrasound transducers on polymer-based microchips," in Proceedings of the 2017 IEEE International Ultrasonics Symposium (IUS), Washington, DC (September 6–9, 2017).

[9]R. P. Moiseyenko and H. Bruus, "Whole-system ultrasound resonances as the basis for acoustophoresis in all-polymer microfluidic devices," Phys. Rev. Appl. 11, 014014 (2019).

[10]A. Mueller, A. Lever, T. V. Nguyen, J. Comolli, and J. Fiering, "Continuous acoustic separation in a thermoplastic microchannel," J. Micromech. Microeng. 23(12), 125006 (2013).

[11]R. Barnkob, P. Augustsson, T. Laurell, and H. Bruus, "Measuring the local pressure amplitude in microchannel acoustophoresis," Lab Chip 10(5), 563–570 (2010).

[12]P. Augustsson, R. Barnkob, S. T. Wereley, H. Bruus, and T. Laurell, "Automated and temperature-controlled micro-PIV measurements

4290   J. Acoust. Soc. Am. 149 (6), June 2021

Lickert et al.

enabling long-term-stable microchannel acoustophoresis character-ization," Lab Chip **11**(24), 4152–4164 (2011).

[13]P. B. Muller, M. Rossi, A. G. Marín, R. Barnkob, P. Augustsson, T. Laurell, C. J. Kähler, and H. Bruus, "Ultrasound-induced acoustophoretic motion of microparticles in three dimensions," Phys. Rev. E **88**(2), 023006 (2013).

[14]B. Hammarström, M. Evander, H. Barbeau, M. Bruzelius, J. Larsson, T. Laurell, and J. Nilsson, "Non-contact acoustic cell trapping in disposable glass capillaries," Lab Chip **10**(17), 2251–2257 (2010).

[15]A. Lenshof, M. Evander, T. Laurell, and J. Nilsson, "Acoustofluidics 5: Building microfluidic acoustic resonators," Lab Chip **12**, 684–695 (2012).

[16]W. N. Bodé and H. Bruus, "Numerical study of the coupling layer between transducer and chip in acoustofluidic devices," J. Acoust. Soc. Am. **149**(5), 3096–3105 (2021).

[17]W. N. Bodé, L. Jiang, T. Laurell, and H. Bruus, "Microparticle acousto-phoresis in aluminum-based acoustofluidic devices with PDMS covers," Micromachines **11**(3), 292 (2020).

[18]A. Tahmasebipour, L. Friedrich, M. Begley, H. Bruus, and C. Meinhart, "Toward optimal acoustophoretic microparticle manipulation by exploit-ing asymmetry," J. Acoust. Soc. Am. **148**(1), 359–373 (2020).

[19]N. R. Skov, J. S. Bach, B. G. Winckelmann, and H. Bruus, "3D modeling of acoustofluidics in a liquid-filled cavity including streaming, viscous boundary layers, surrounding solids, and a piezoelectric transducer," AIMS Math. **4**, 99–111 (2019).

[20]J. S. Bach and H. Bruus, "Theory of pressure acoustics with viscous boundary layers and streaming in curved elastic cavities," J. Acoust. Soc. Am. **144**, 766–784 (2018).

[21]M. Settnes and H. Bruus, "Forces acting on a small particle in an acousti-cal field in a viscous fluid," Phys. Rev. E **85**, 016327 (2012).

[22]N. R. Skov, P. Sehgal, B. J. Kirby, and H. Bruus, "Three-dimensional numerical modeling of surface-acoustic-wave devices: Acoustophoresis of micro- and nanoparticles including streaming," Phys. Rev. Appl. **12**, 044028 (2019).

[23]P. B. Muller and H. Bruus, "Numerical study of thermoviscous effects in ultrasound-induced acoustic streaming in microchannels," Phys. Rev. E **90**(4), 043016 (2014).

[24]J. T. Karlsen, P. Augustsson, and H. Bruus, "Acoustic force density acting on inhomogeneous fluids in acoustic fields," Phys. Rev. Lett. **117**, 114504 (2016).

[25]J. T. Karlsen and H. Bruus, "Forces acting on a small particle in an acous-tical field in a thermoviscous fluid," Phys. Rev. E **92**, 043010 (2015).

[26]W. Slie, A. Donfor, Jr., and T. Litovitz, "Ultrasonic shear and longitudinal measurements in aqueous glycerol," J. Chem. Phys. **44**(10), 3712–3718 (1966).

[27]L. Negadi, B. Feddal-Benabed, I. Bahadur, J. Saab, M. Zaoui-Djelloul-Daouadji, D. Ramjugernath, and A. Negadi, "Effect of temperature on density, sound velocity, and their derived properties for the binary sys-tems glycerol with water or alcohols," J. Chem. Thermodyn. **109**, 124–136 (2017).

[28]N.-S. Cheng, "Formula for the viscosity of a glycerol-water mixture," Ind. Eng. Chem. Res. **47**(9), 3285–3288 (2008).

[29]B. Hartmann and J. Jarzynski, "Polymer sound speeds and elastic con-stants," Naval Ordnance Laboratory Report NOLTR 72-269, US Naval Ordnance Laboratory, White Oak, MD, 1972.

[30]D. Christman, "Dynamic properties of poly(methylmethacrylate) (PMMA) (Plexiglas)," Report No. DNA 2810F, MSL-71-24, General Motors Technical Center, Warren, MI, 1972.

[31]H. Sutherland and R. Lingle, "Acoustic characterization of polymethyl methacrylate and three epoxy formulations," J. Appl. Phys. **43**(10), 4022–4026 (1972).

[32]H. Sutherland, "Acoustical determination of shear relaxation functions for polymethyl methacrylate and Epon 828-Z," J. Appl. Phys. **49**(7), 3941–3945 (1978).

[33]J. Carlson, J. van Deventer, A. Scolan, and, and C. Carlander, "Frequency and temperature dependence of acoustic properties of polymers used in pulse-echo systems," in *Proceedings of the IEEE Symposium on Ultrasonics, 2003*, Honolulu, HI (October 5–8, 2003), Vol. 1, pp. 885–888.

[34]A. Simon, G. Lefebvre, T. Valier-Brasier, and R. Wunenburger, "Viscoelastic shear modulus measurement of thin materials by interf-ometry at ultrasonic frequencies," J. Acoust. Soc. Am. **146**(5), 3131–3140 (2019).

[35]H. T. Tran, T. Manh, T. F. Johansen, and L. Hoff, "Temperature effects on ultrasonic phase velocity and attenuation in Eccosorb and PMMA," in *Proceedings of the 2016 IEEE International Ultrasonics Symposium (IUS)*, Tours, France (September 18–21, 2016), pp. 1–4.

[36]P. Hahn and J. Dual, "A numerically efficient damping model for acoustic resonances in microfluidic cavities," Phys. Fluids **27**, 062005 (2015).

[37]COMSOL Multiphysics 5.5 (2019), http://www.comsol.com (Last viewed 7 May 2021).

[38]P. B. Muller, R. Barnkob, M. J. H. Jensen, and H. Bruus, "A numerical study of microparticle acoustophoresis driven by acoustic radiation forces and streaming-induced drag forces," Lab Chip **12**, 4617–4627 (2012).

[39]M. Bora and M. Shusteff, "Efficient coupling of acoustic modes in micro-fluidic channel devices," Lab Chip **15**(15), 3192–3202 (2015).

[40]See supplementary material at https://www.scitation.org/doi/suppl/10.1121/10.0005113 for four animations of the simulated 1.17-MHz mode shown in Fig. 3 and one video of the experimental particle focusing corresponding to Fig. 6.

[41]R. Barnkob, I. Iranmanesh, M. Wiklund, and H. Bruus, "Measuring acoustic energy density in microchannel acoustophoresis using a simple and rapid light-intensity method," Lab Chip **12**, 2337–2344 (2012).